

# Numerical simulations of the jetted tidal disruption event Swift J1644+57

Petar Mimica<sup>1</sup>, Miguel A. Aloy<sup>1</sup>, Dimitrios Giannios<sup>2</sup>, and Brian D. Metzger<sup>3</sup>

<sup>1</sup>Departamento de Astronomía y Astrofísica, Universidad de Valencia, 46100, Burjassot, Spain

<sup>2</sup>Department of Physics and Astronomy, Purdue University, 525 Northwestern venue, West Lafayette, IN 47907, USA

<sup>3</sup>Columbia Astrophysics Laboratory, Columbia University, New York, NY, 10027, USA

September 26, 2018

## Abstract

In this work we focus on the technical details of the numerical simulations of the non-thermal transient Swift J1644+57, whose emission is probably produced by a two-component jet powered by a tidal disruption event. In this context we provide details of the coupling between the relativistic hydrodynamic simulations and the radiative transfer code. First, we consider the technical demands of one-dimensional simulations of a fast relativistic jet, and show to what extent (for the same physical parameters of the model) do the computed light curves depend on the numerical parameters of the different codes employed. In the second part we explain the difficulties of computing light curves from axisymmetric two dimensional simulations and discuss a procedure that yields an acceptable tradeoff between the computational cost and the quality of the results.

## 1 Introduction

Tidal disruption events (TDE) of stars by massive black holes [1, 2, 3] provide one of the ways to detect an inactive massive black hole in the center of a galaxy. Stars whose orbit brings them too close to a black hole can be disrupted and a large fraction of their mass can be accreted. This sudden accretion event is expected to produce a luminous UV and X-ray TDE flare [4, 5]. It has recently been argued that TDEs can also produce jets [6, 7, 8]. These jets are expected to be detectable due to their non-thermal emission, and in radio they are likely to appear as transients that peak on the timescales of about a year [6, 9] after the tidal disruption.

Swift J1644+57 (SwJ1644 in the rest of the article) is a non-thermal transient detected on March 28th. 2011 [10, 11, 12]. It is thought to be prototype of a jetted TDE (jTDE). Its radio emission [13, 14, 15] is long-lived and complex. One of the first attempts to explain the radio emission of Swift J1644+57 using one-dimensional models and relativistic hydrodynamic simulations [16] assumed that the emission is coming from the shocks that form when the jet interacts with the circumnuclear medium (CNM). This model is more analogous to a GRB

afterglow than to an AGN<sup>1</sup>. While the model was successful in explaining the first few weeks of SwJ1644 radio emission, it turns out that the long-term emission is not easily accounted for by a radio afterglow from a single ultrarelativistic, narrow jet. The reason for this is that the source rebrightened after  $\gtrsim 150$  days, the time at which the afterglow model predicted a steady decline [14, Figure 1]. The late time rebrightening implies that additional energy is injected in the external shock months after the burst [14]. This may happen if, for instance, the jTDE is accompanied by a powerful mildly relativistic component [18]<sup>2</sup>.

In this contribution we focus on the numerical and technical aspects of jTDE modeling. In Section 2 we describe the numerical codes used in the calculations and how they depend on each other. The Section 3 gives an overview of computational requirements and their consequences on the kind of models that we were able to produce. The discussion and summary is given in the Section 4.

## 2 Numerical codes

SwJ1644 is a distant object (its redshift is  $z = 0.354$  [10]), and is thus too small to be resolved in great detail<sup>3</sup>. Thus, the only direct observations that we have are the total fluxes for different times and frequencies (i.e., multiwavelength light curves). Nevertheless, when simulating this source we need to construct a detailed, resolved model of the SwJ1644 jet, simulate its dynamics, compute its resolved emission, and only in the final stage integrate the resolved emission to compute the total flux to be compared to observations. In order to achieve this we use two numerical codes so that the output of the first code (*MARGENESIS*) is used as an input to the second one (*SPEV*). The former simulates the jet dynamics, while the latter computes its emission.

### 2.1 Relativistic hydrodynamics simulations

*MARGENESIS* is a code developed to solve the equations of relativistic numerical (magneto) hydrodynamics *in the laboratory frame* (i.e., a frame at rest with respect to the distant source)<sup>4</sup>. The code is massively parallelized using MPI<sup>5</sup> and OpenMP<sup>6</sup> libraries, and uses the parallel HDF5<sup>7</sup> library for file input and output. We employ a method of lines for our simulations in which the spatial reconstruction is based on the third order PPM reconstruction routines [22], and the time update is performed by means of a third order TVD Runge-Kutta scheme [23]. Numerical fluxes are evaluated with the Marquina flux formula [24]. We simulate SwJ1644 in two dimensions assuming axisymmetry and discretize the computational domain using spherical coordinates. The black hole is assumed to be located at the origin and the TDE occurs at scales that are much smaller than the ones we consider in our work (we simulate neither the TDE nor the jet launching). We set the beginning of the numerical grid at  $\sim 10^{16}$  cm. The jet is injected

---

<sup>1</sup>Interested readers can find details of the model based on the AGN jet-disc symbiosis in Section 2.1 of [17]. We note that [17] assume that the origin of the emission is *internal* to the jet, as opposed to the *external* emission that we advocate.

<sup>2</sup>For an overview of alternative explanations for late-time rebrightening see Section 2.2 of [18].

<sup>3</sup>According to our numerical models we predict that SwJ1644 may become resolvable by Very Long Baseline Interferometry sometime in the next few years (see Figure 13 in [18]).

<sup>4</sup>Interested readers can find details about the original *GENESIS* in [19], its extension to relativistic magnetohydrodynamics in [20], and the current parallelized version (*MARGENESIS*) that handles ultrarelativistic magnetized outflows in [21].

<sup>5</sup>MPI (Message Passing Interface) is used for distributed-memory parallelism, see <http://www.mpi-forum.org>

<sup>6</sup>OpenMP (Open Multi-Processing) is used for shared-memory parallelism, see <http://openmp.org>.

<sup>7</sup>HDF5 (Hierarchical Data Format) is used to store and manage large datasets, see <http://hdfgroup.org>.

through the inner boundary in an angular interval  $[0, \theta_j]$ , assuming a constant Lorentz factor  $\Gamma_j$ , and a luminosity whose time dependence is  $L_j(t) = L_{j,0} \max[1, (t/t_0)]^{-5/3}$ .  $t_0$  is the time during which the jet luminosity is constant, and the peak luminosity  $L_{j,0}$  is computed from the total jTDE energy  $E_{\text{ISO}}$  through  $L_{j,0} = 2E_{\text{ISO}}/(5t_0)$ . The jet interacts with a CNM that is assumed to be at rest with a density profile  $\rho_{\text{cnm}} = n_{18}m_p(r/10^{18}\text{cm})^{-k}$ , where  $m_p$  is the proton mass,  $n_{18}$  is the particle number density at  $10^{18}$  cm and  $k$  is the power-law index of the density profile. We assume that initially both the jet and the external medium are cold. During the simulation we periodically store the snapshots of the computational grid in order to obtain a sufficient coverage of the jet-CNM interaction to be able to compute the resulting emission with sufficient precision (see Section 3).

## 2.2 Radiative transfer

Once the relativistic hydrodynamics simulation has finished, the snapshots it produced are used by the code *SPEV* to compute the emission. The spatial distribution of the hydrodynamics variables needs to be stored with sufficient frequency because of the space-time transformations that need to be performed to compute the observable radiation in the (distant) *observer frame*. *SPEV*[25] is designed to process an arbitrary number of pre-computed sets of hydrodynamic states of the fluid (i.e., density, pressure, positions, velocities, magnetic field) and to compute the resulting non-thermal emission. The procedure can be summarized as follows:

1. **Injection:** *SPEV* uses a set of Lagrangian particles (LPs) as a representation of the emitting volumes. Each LP has a defined position, shape and velocity. Attached to it there is a representation of the non-thermal electron (NTE) energy distribution. In *SPEV*, new LPs are created each time a snapshot is processed. The position of the shock fronts that form as a consequence of the jet-CNM interaction is detected, and LPs are injected into the shocked fluid immediately behind the front. Since the actual process of particle acceleration occurs on temporal and spatial scales far below the ones we are able to simulate (see e.g., [26] for a recent review), we use a phenomenological model to link the fluid state with NTE distribution. The model we use is a standard one [27]: the energy contained in the NTEs and in the stochastic magnetic field are assumed to be fractions  $\epsilon_e$  and  $\epsilon_B$  of the shocked fluid thermal energy. The injection spectrum is assumed to be a power-law in energy  $n(\gamma) \propto \gamma^{-p}$ , where  $p$  is the power-law index and  $\gamma$  is the NTE Lorentz factor. We determine the normalization and energy cutoffs of the distribution using a numerical procedure described in detail in Sections 3.2 and 3.3 of [28].
2. **Transport, evolution and emission:** As it processes the snapshots, *SPEV* transports the injected LPs, assuming that after they have been injected they move with the fluid. An exception are the newly injected LPs: between the snapshot in which the particle is injected and the subsequent one the two edges parallel to the shock front are assumed to move with different velocities (one with the velocity of the shocked fluid and the other one with the faster velocity of the shock front). This ensures that new LPs correctly represent the increase in the volume due to newly shocked fluid, regardless of the numerical resolution or the frequency with which snapshots are stored. Simultaneously, the NTE energy losses due to synchrotron radiation, as well as the energy gains(losses) due to adiabatic compression(expansion) are taken into account:

$$\frac{d\gamma}{dt} = \frac{1}{3} \frac{d \ln \rho}{dt} \gamma - \frac{4}{3} \frac{c\sigma_T}{m_e c^2} (u_B + u_{\text{rad}}) \gamma^2 \quad (1)$$

where  $t$ ,  $\rho$ ,  $u_B$  and  $u_{\text{rad}}$  are the time, fluid density, magnetic field energy density and external radiation field energy density (all measured in the LP frame). Section 3.2 of [25]

describes an efficient numerical algorithm for solving Eq. 1 for each NTE distribution in each LP. At the same time that the particles are evolved, their non-thermal emission is computed (see Section 4 of [25] for a description of an efficient numerical algorithm for computing synchrotron emission and absorption coefficients, and Section A.2.1 of the same paper for a description of the way particles in two-dimensional axisymmetric models can be used to represent three-dimensional emitting volumes). The coefficients computed in this step are stored in a global array that is used in the final step.

3. **Solving the radiative transfer equation:** After all the snapshots have been processed and the emission from all LPs has been computed for all times, the time- and frequency-dependent emission can be computed. We assume that there is a virtual screen (“virtual detector”, VD) located in front of the source, and the goal is to compute the intensity in each of the virtual pixels of the VD. This is done by solving the radiative transfer equation

$$\frac{dI_\nu}{ds} = j_\nu - \alpha_\nu I_\nu, \quad (2)$$

where  $I_\nu$ ,  $j_\nu$  and  $\alpha_\nu$  are the specific intensity, emissivity and absorption coefficient.  $s$  is the distance along the line of sight from the jet to a particular pixel and it relates the simulation time  $t$  to the time of observation  $T$  by  $t = T + (D - s)/c$ , where  $D$  is the distance from the VD to the source. In other words, for a given  $T$  and  $t$ ,  $s$  is the distance of a LP from which radiation is observed at time  $T$  if that LP is emitting at a time  $t$ . We note that Eq. 2 needs to be solved in such a way that  $s$  is monotonously increasing from the jet towards the VD. Therefore, after all the snapshots have been processed, the emission and absorption coefficients need to be sorted according to their  $s$  and then Eq. 2 is solved for each pixel.

In practice the positions of LPs in steps (i) and (ii) are stored in a set of (large) intermediate files (“preprocessor” files). A postprocessor executes the radiation part of step (ii) by reading the preprocessor files and storing the coefficients in memory. After all preprocessor files have been postprocessed, the step (iii) is executed. Both preprocessor and postprocessor parts of *SPEV* are parallelized using OpenMP. The postprocessor, in particular, needs to be run on a machine with enough shared memory<sup>8</sup> because all information produced in step 2 needs to be held in memory for the step 3 to correctly compute the intensities.

### 3 Simulations of Swift J1644+57 jet

As mentioned in Section 2.1, we model SwJ1644 jet in two-dimensions. However, as will be explained in this Section, the total cost in terms of computing time, disk storage and working memory of each two-dimensional simulation is high. Therefore, we first perform a number of much less costly tests using a one-dimensional approximation to two-dimensional models. The goal of those tests is to determine the values of a number of the parameters of the numerical simulation for which the results are satisfactory. Afterward, the two-dimensional simulations are performed using the values determined in one-dimensional tests.

#### 3.1 One-dimensional tests

Using *MARGENESIS* we simulate one-dimensional spherically symmetric jets. For the purpose of computing their emission with *SPEV* we assume that their opening angles are  $\theta_j$ . We fix all

---

<sup>8</sup>Interested readers should consult Chapter 4 of [29] for a detailed description of the optimized memory management in *SPEV*.

the physical parameters of the jet ( $E_{\text{ISO}} = 4 \times 10^{54}$  erg,  $\Gamma_j = 10$ ,  $\theta_j = 0.1$  rad,  $t_0 = 5 \times 10^5$  s) and of the external medium ( $n_{18} = 60$  cm $^{-3}$ ,  $k = 1.5$ ). This corresponds to the inner relativistic component of the two-component jet in [18]. The numerical parameters that will be varied are<sup>9</sup>:

- $\Delta T_{\text{snap}}$ : time interval between snapshots (*MRGENESIS*)
- $\Delta r$ : radial resolution (*MRGENESIS*)
- $\Delta \theta$ : angular resolution (*MRGENESIS*<sup>10</sup>)
- $N_b$ : number of NTE energy distribution bins (*SPEV*)
- $n_x$ : resolution of the virtual detector (*SPEV*<sup>11</sup>)

We choose as a default set of parameters  $\Delta T_{\text{snap}} = 8.3 \times 10^4$  s,  $\Delta r = 5 \times 10^{13}$  cm,  $\Delta \theta = 2 \times 10^{-3}$  rad,  $N_b = 32$ ,  $n_x = 1000$ . We follow the jet evolution until  $\sim 6.7 \times 10^8$  seconds. During the first  $1.3 \times 10^8$  seconds the snapshots are output every  $\Delta T_{\text{snap}}$ , and afterward the time interval increases by a factor 1.002 after every snapshot is output.

Fig. 3.1 shows the light curves for the default model evaluated at 1.4 GHz (red line) and the consequence of variations in the resolution of the hydrodynamic models, i.e., as a result of changing  $\Delta r$ . As can be seen, relatively small differences of the order of a percent are visible at early times and after the light curve maximum. The top right panel in Fig. 3.1 shows the result of changing angular resolution. Here the differences are somewhat larger, especially when comparing the lowest and highest resolution ( $\sim 4\%$  at peak). The middle left panel in Fig. 3.1 shows how the results depend on the number of bins in which NTE energy distribution of each LP is discretized. We see that the convergence is only achieved for  $N_b \gtrsim 32$ . In the middle right panel we can see that the oscillations at early times are due to poor VD resolution. The angular size of the jet is very small at those times and it is only properly resolved for  $n_x \sim 10^4$  for a linear pixel distribution (covering the interval  $[0, 5 \times 10^{18}$  cm]), and  $n_x \sim 10^3$  for a logarithmic one (covering the interval  $[10^{12}$  cm,  $5 \times 10^{18}$  cm]). In the next section we will explain how we solved the problem of noise for 2D simulation light curves, especially the off-axis ones where it is not feasible to distribute the VD pixels logarithmically. Finally, the bottom left panel shows the (weak) dependence on  $\Delta T_{\text{snap}}$ .

### 3.2 Two-dimensional simulations

In the previous section we showed how the light curves change as the five principal numerical parameters are changed. Most importantly for the 2D simulations, with the previous tests we have already obtained a very good proxy for the largest values of  $\Delta r$  and  $\Delta \theta$  we can use in order to reduce the computational cost without compromising the accuracy of the results. In the final simulations showed in [18] we used  $\Delta r = 4 \times 10^{14}$  cm and  $\Delta \theta \simeq 2.6 \times 10^{-3}$  rad. In this section we discuss the technical challenges of computing the emission even from these relatively low-resolution hydrodynamic simulations.

The complete two-dimensional evolution is stored in 2412 snapshots. It was fortunate that HDF5 format permits data compression so that the compressed snapshots occupy  $\simeq 460$  Gbytes.

---

<sup>9</sup>We note that the results of a limited number of numerical tests have also been presented in Appendix A of [18], but here we perform an exhaustive analysis.

<sup>10</sup>When performing one-dimensional simulations we create mock two-dimensional snapshots using  $\Delta \theta$  as angular cell size.

<sup>11</sup>In these one-dimensional tests we assume that the jet is observed on-axis (viewing angle is 0 degrees), so that its emission is axially-symmetric and we only need to compute the emission along VD x-axis. For off-axis observations a (much more costly) two-dimensional VD calculation is performed [18, Section 5.2]. We comment in detail on technical challenges of 2D simulations in next section.

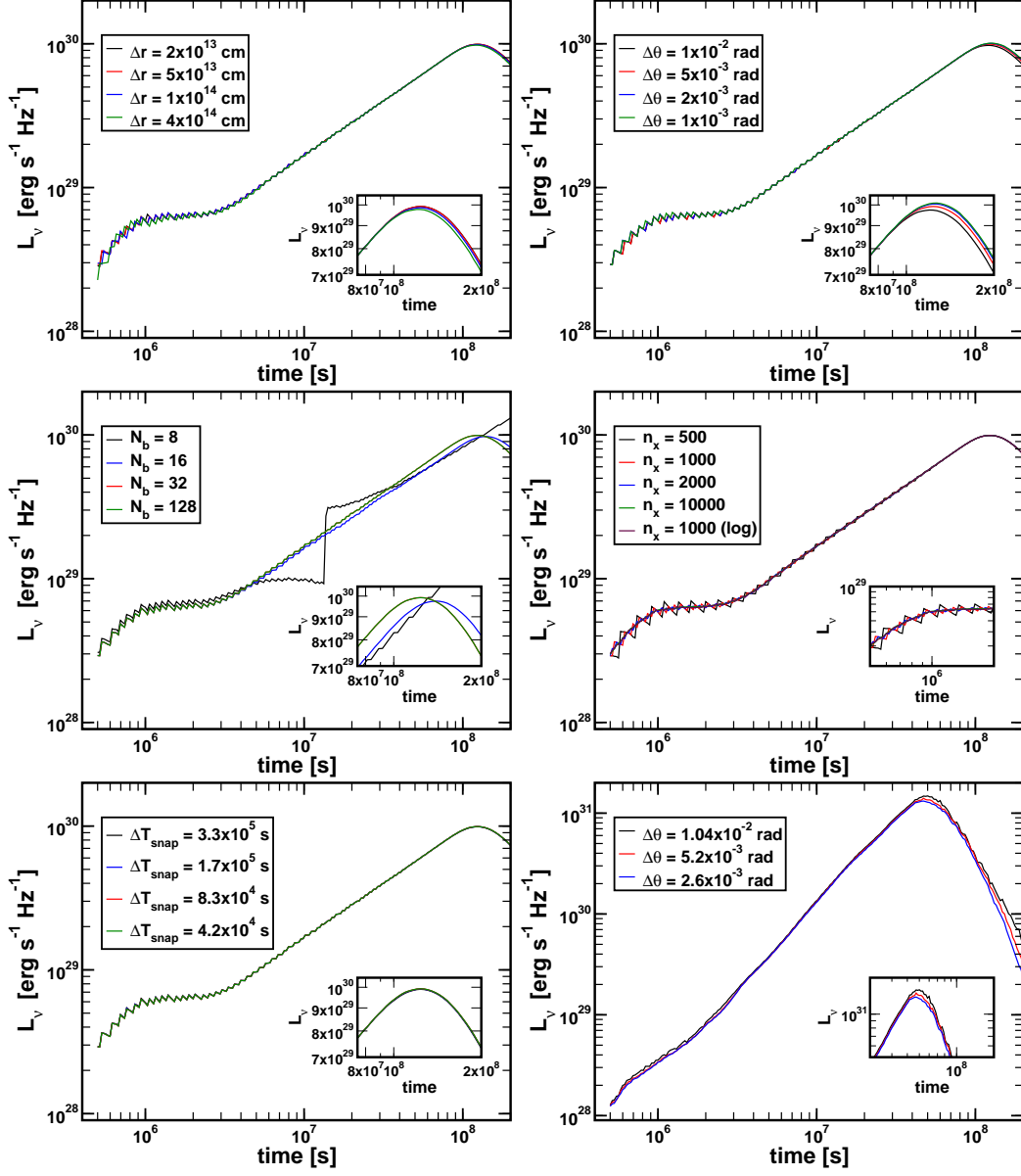


Figure 1: 1.4 GHz radio light curves of one-dimensional tests (Section 3.1). The default model is shown in red. The insets show the zoom-in around the light curve maximum. *Top left panel:* Variations in  $\Delta r$ . *Top right panel:* Variations in  $\Delta \theta$ . *Middle left panel:* Variations in the number of bins  $N_b$ . Note that  $N_b = 32$  and  $N_b = 128$  curves overlap. *Middle right panel:* Variations in the number of VD pixels. Note that the curves for  $n_x = 10^4$  and  $n_x = 10^3$  with a logarithmic distribution of pixels overlap. *Bottom left panel:* Variations in  $\Delta T_{\text{snap}}$ . *Bottom right panel:* Emission from two dimensional two-component jet for different effective angular resolutions (see Section 3.2).

Running the preprocessor with the default parameters of Section 3.1 produces 160 (compressed) intermediate files. Each of the first 159 files contains the positions, geometry, velocity, magnetic field and the 32 bins of the NT energy distribution of  $2.5 \times 10^6$  LPs, while the last file only contains  $\simeq 1.9 \times 10^6$  LPs. This means that in total there are  $\simeq 4 \times 10^8$  two-dimensional emitting LPs in step (ii) of the *SPEV* algorithm (see Section 2.2). Since each of the LPs has to be converted to a three-dimensional emitting volume, it may contribute to multiple VD pixels and also to multiple observing times, we soon realized that the realistic upper limit of  $\lesssim 1$  TByte of RAM on our shared memory machine<sup>12</sup> would not be enough to compute off-axis images at full resolution. A remedy to this problem was to artificially reduce the angular resolution when preprocessing the hydrodynamic snapshots by a factor of 2 or 4 (this would roughly correspond going from the second-best to third- or fourth-best angular resolution in top left panel in Figure 3.1.). This reduces the number of emitting volumes so that even off-axis radiative transfer calculations could be performed.

### 3.2.1 On-axis light curves

For the purposes of the numerical tests we computed the on-axis light curves (in complete analogy to the tests presented in Section 3.1). Bottom right panel in Figure 3.1 shows on-axis light curves using the full angular resolution, as well as the result of degrading it by factors of 2 and 4.

In Figure 2 we show a subset of the data that *SPEV* stores when postprocessing the intermediate files. In this particular case we show all the contributions to the emission at  $T = 1.4 \times 10^6$  seconds and at 15.4 GHz. The data shown originates from LPs emitting at different times from different positions (the lower the value of  $y$  the earlier the LP had to emit for it to be observed at  $1.4 \times 10^6$  seconds). In other words, what is shown does not correspond to one particular snapshot of the jet evolution. Nevertheless, we know that the edge of the emitting region corresponds to the position of the bow shock of the jet. We also see in the bottom right panel in Figure 2 that a small region behind the shock is optically thin and most of the contribution to the emission comes from this region and from the surface at which the emission becomes optically thin (the transition between light and dark blue regions). Using this type of analysis it is possible to understand, among other things, why the inverse Compton cooling of the electrons is not very efficient at low frequencies (though it may be important for higher frequency observations of SwJ1644, see [30]): the electrons cool after being accelerated by the shock, but since they are advected behind it, once they enter the opaque region (dark blue), they stop contributing to the observed emission. Therefore the observer does not see a large effect of the inverse Compton cooling [18, Section 4.1.2].

### 3.2.2 Off-axis light curves

Here we comment on the procedure we use to reduce the numerical noise that shows at early times (Figure 3.1). As was commented in Section 3.1, the jet is small at early times, so that at a typical resolution of 1000 points per spatial direction it is very poorly resolved by the VD. Due to memory limitations we were not able to use VD resolution of  $10000^2$ . However, the resolutions of  $1000^2$  pixels were feasible. Therefore, we adopted the following procedure:

1. Pre-determine the jet viewing angle  $\theta_{\text{obs}}$  and the times  $T_i$  ( $i = 1, \dots, n_t$ ) at which it is to be observed.
2. Compute the radio images using  $1000 \times 1000$  VD for each  $T_i$  in a single calculation.

---

<sup>12</sup>We use the machine *Lluís Vives* hosted at the University of Valencia. It has 30 Xeon 7500 hexacore CPUs clocked at 2.67 GHz and almost 1 TBytes of RAM. For more information see [http://www.uv.es/siuv/cas/zcalculo/calculouv/des\\_vives.wiki](http://www.uv.es/siuv/cas/zcalculo/calculouv/des_vives.wiki) (in Spanish).

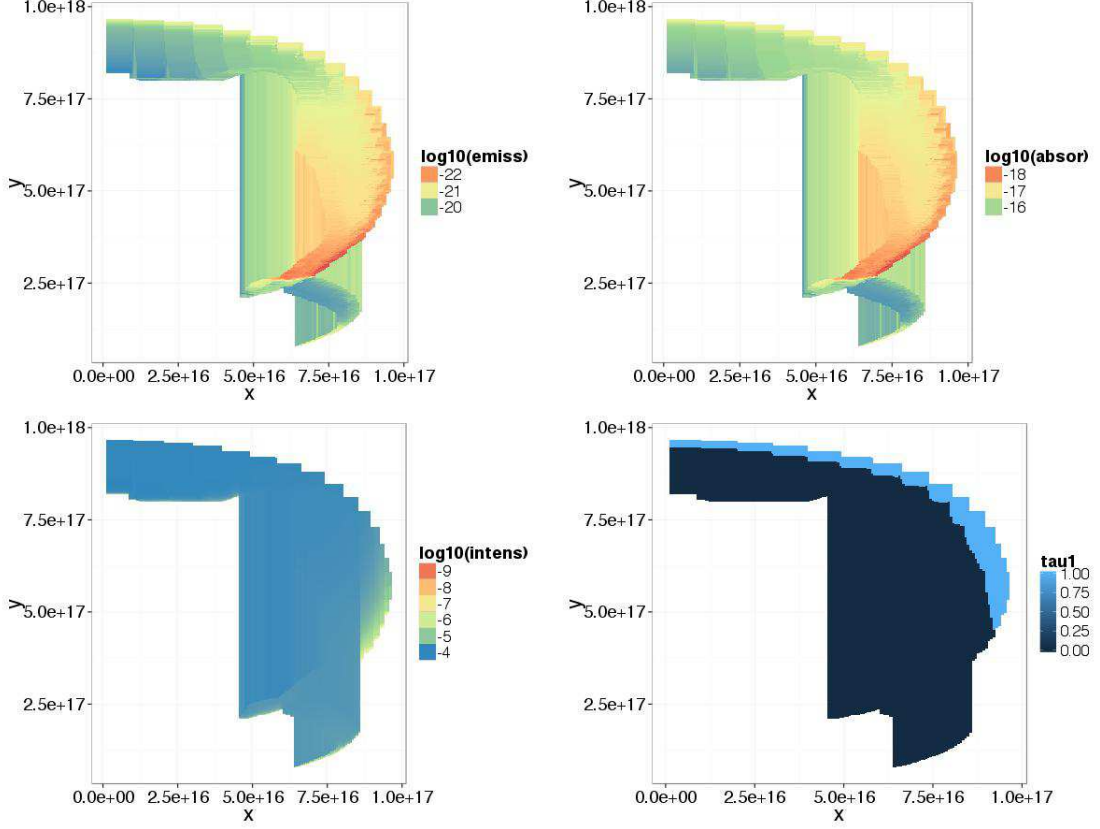


Figure 2: Observer frame simultaneous emission, absorption, intensity and optical depth that contribute to the emission at  $T = 1.4 \times 10^6$  seconds at 15.4 GHz. *Top left:* synchrotron emissivity in  $\text{erg s}^{-1} \text{cm}^{-3} \text{Hz}^{-1}$ . *Top right:* synchrotron self-absorption in  $\text{cm}^{-1}$ . *Bottom left:* specific intensity in  $\text{erg s}^{-1} \text{cm}^{-2} \text{Hz}^{-1}$ . The intensity is the result of integrating Equation 2 from bottom to top for each vertical line. *Bottom right:* optical depth measured from the observer (integral of the absorption from top to bottom along vertical lines). The light blue colored region denotes the part of the emitting volume that is transparent, while the emission in the dark blue region is absorbed. As explained in Section 3.2.1, the information displayed here is a subset of the data stored in the global array used by *SPEV* to compute the intensity in each pixel (see Section 2.2). The luminosity is obtained by integrating the intensity along vertical lines in the top right panel (taking into account that the emission is axially symmetric).



3. For each  $T_i$ , determine the rectangle that contains 99.99% of the emission. Then expand the rectangle by a safety margin.
4. For each  $T_i$ , independently re-compute the radio image by limiting the VD to the rectangle computed in the previous step, but using the resolution  $1000 \times 1000$ .

The above procedure enables us to compute the emission from early times without numerical artifacts<sup>13</sup>. The tradeoff is that we need to postprocess the intermediate files multiple times: once in step (ii) and then additional  $n_t$  times in step (iv). The computing time does not necessarily scale as  $n_t$  since, for each  $T_i$ , the emission and absorption coefficients are only computed from those emitting volumes that contribute to the emission, while the rest (typically corresponding to most of the volume of the model) are ignored. This is made efficient by indexing the intermediate files. For a given observing angle the calculations at 8 different observing frequencies last  $\simeq 3 - 5$  days.

## 4 Summary

In this contribution we have discussed the technical details of the one and two dimensional simulations of the SwJ1644 jet. In Section 2 we explain in detail how the relativistic hydrodynamic simulations are coupled to the radiative transfer code to produce the synthetic observations (light curves) that can be directly compared to the observations. In Section 3.1 we show that many one-dimensional tests can be used to probe the sensitivity of the computed light curves on the resolution of the hydrodynamic simulations, on the frequency of stored snapshots, on the resolution of the discretization in energy space and of the virtual detector. The results obtained helped to determine the resolution of the two dimensional simulation so that its computational cost is acceptable, but also so that the final light curves are as free of numerical artifacts as possible. This procedure has been successful in enabling us to produce a viable two-component jet model of the SwJ1644 jet.

## Acknowledgements

PM and MAA acknowledge the support from the European Research Council (grant CAMAP-259276), and the partial support of grants AYA2013-40979-P, PROMETEO-II-2014-069 and SAF2013-49284-EXP. DG acknowledges support from the NASA grant NNX13AP13G. BDM acknowledges support from the NSF grant AST-1410950 and the Alfred P. Sloan Foundation. We thankfully acknowledge the computer resources, technical expertise and assistance provided by the "Centre de Càlcul de la Universitat de València" through the use of *Lluís Vives* cluster and *Tirant*, the local node of the Spanish Supercomputation Network. We use the open source software packages *Grace*<sup>14</sup> and *ggplot2*<sup>15</sup> to produce the graphics in this paper.

## References

- [1] Lacy J H, Townes C H and Hollenbach D J *ApJ* **262**, 120
- [2] Rees M J 1988 *Nature* **333**, 523

---

<sup>13</sup>Figures 12-14 in [18] were computed using this procedure. Note that in Figure 14 in [18] the jet size in the upper panels is  $\simeq 3 - 5$  times smaller than in the lower panels, but all are computed using the same VD resolution.

<sup>14</sup><http://plasma-gate.weizmann.ac.il/Grace>

<sup>15</sup><http://ggplot2.org>

- [3] Evans C R and Kochanek C S 1989 *ApJ* **346**, 13
- [4] Strubbe L E and Quataert E 2009 *MNRAS* **400**, 2070
- [5] Lodato G and Rossi E M 2011 *MNRAS* **410** 359
- [6] Giannios D and Metzger B D 2011 *MNRAS* **416**, 20102
- [7] Krolik J H and Piran T 2012 *ApJ* **749**, 92
- [8] Tchekhovskoy A, Metzger B D, Giannios D and Kelley L Z 2014 *MNRAS* **437**, 2744
- [9] Metzger B D, Williams P K G and Berger E 2015 *ApJ* **806**, 224
- [10] Bloom J S *et al.* 2011 *Science* **333**, 203
- [11] Burrows D N *et al.* 2011 *Nature* **476**, 421
- [12] Levan A J *et al.* 2011 *Science* **333**, 109
- [13] Zauderer B A *et al.* 2011 *Nature* **476**, 425
- [14] Berger E *et al.* 2012 *ApJ* **748**, 36
- [15] Zauderer B A *et al.* 2013 *ApJ* **767**, 152
- [16] Metzger B D, Giannios D and Mimica P 2012 *MNRAS* **420**, 3528
- [17] van Velzen S, K rding E and Falcke H 2011 *MNRAS* **417**, L51
- [18] Mimica P, Giannios D, Metzger B D and Aloy M A 2015 *MNRAS* **450**, 2824
- [19] Aloy M A, Ib    ez J M, Mart   J M and M  ller E 1999 *ApJS* **122**, 151
- [20] Leismann T *et al.* 2005 *A&A* **436**, 503
- [21] Mimica P, Giannios D and Aloy M A 2009 *A&A* **494**, 879
- [22] Colella P and Woodward P R 1984 *JCP* **54**, 174
- [23] Shu C W and Osher S J 1984 *JCP* **77**, 439
- [24] Donat R, Font J A, Ib    ez J M and Marquina A 1988 *JCP* **146**, 58
- [25] Mimica P *et al.* 2009 *ApJ* **696**, 1142
- [26] Sironi S, Keshet U and Lemoine M 2015 *Space Science Reviews* **191**, 519
- [27] Sari R, Piran T and Narayan R 1998 *ApJ* **49**, L17
- [28] Mimica P and Aloy M A 2012 *MNRAS* **421**, 2635
- [29] Aloy C., 2013, masters thesis, Univ. Polit. de Valencia., <https://riunet.upv.es/handle/10251/35350>
- [30] Kumar P, Barniol Duran R, Bo  njak    and Piran T 2013 *MNRAS* **445**, 3919